Chinese Chemical Letters 37 (2026) 110711

Contents lists available at ScienceDirect

Chinese Chemical Letters

journal homepage: www.elsevier.com/locate/cclet

Electronegativity-oriented coordination regulation of main-group metal single-atom catalysts for oxygen reduction to H_2O_2: A combined study of first-principles and machine learning

Hao Chen[a], Haiyuan Liao[a], Qi Zhou[b], Yang Liu[a,*], Guojun Liu[b,*], Yuan Yao[a,*]

[a] MIIT Key Laboratory of Critical Materials Technology for New Energy Conversion and Storage, School of Chemistry and Chemical Engineering, Harbin Institute of Technology, Harbin 150001, China
[b] School of Computer Science and Technology, Harbin Institute of Technology, Harbin 150001, China

ARTICLE INFO

Article history:
Received 8 October 2024
Revised 27 November 2024
Accepted 3 December 2024
Available online 3 December 2024

Keywords:
Density functional theory
Machine learning
Main-group metal single-atom catalyst
Two-electron oxygen reduction reaction
Electronegativity
Coordination environment

ABSTRACT

Electrochemical two-electron oxygen reduction reaction (2e⁻ ORR) is a green and attractive method for hydrogen peroxide synthesis. However, rapid and efficient development of high-performance catalyst remains a great challenge. Different from traditional trial and error methods, this study employs density functional theory and machine learning method to efficiently screen the promising main-group metal single-atom catalysts (SACs) and systematically investigate the influence of electronegativity of coordination atoms on the adsorption behavior of key intermediates in ORR process. It is found that the K SAC with N/B in the first coordination sphere and Sn SAC with N/C in the first coordination sphere and O in the second coordination sphere exhibit both excellent 2e⁻ ORR activity and selectivity by showing extremely low overpotentials of 0.029 V and 0.064 V, respectively, as well as barrier-free processes from *OOH to H_2O_2. Bagging displays prominent advantages among seven popular algorithms because of its ensemble strategy. This provides a low-cost approach for designing and screening electrocatalyst candidates, and it will be informative for experimental study in the future to accelerate the development of catalysts for oxygen reduction and other types of reactions.

© 2025 Published by Elsevier B.V. on behalf of Chinese Chemical Society and Institute of Materia Medica, Chinese Academy of Medical Sciences.

Hydrogen peroxide, as a significant green chemical product, finds widespread application across various sectors [1,2]. With the changing global energy landscape and the growing demand for environmental sustainability, the electrochemical oxygen reduction pathway to produce hydrogen peroxide emerges as an eco-friendly alternative to traditional energy-intensive anthraquinone production method [3–6]. It is highly required to develop high-performance oxygen reduction reaction catalysts in an efficient and economical way [7,8].

Presently, precious metal catalysts are predominantly employed for the two-electron oxygen reduction reaction to produce H_2O_2 (2e⁻ ORR), such as Pt-Hg [9], Pd-Hg [10], and Pd-Au [11]. Nevertheless, the exorbitant cost limited the availability of precious metals. In recent years, the transition metal-based single-atom catalysts (SACs) attract great attention due to the high reactivity and flexible adjustability of the electronic structures [12,13]. However, it is crucial to note that their strong Fenton effect would affect the stability of hydrogen peroxide [14,15]. In contrast, SACs based main-group metals could effectively avoid this Fenton issue. Additionally, these metal elements are abundant in the earth's crust and their s/p electrons could be activated through local coordination, making them highly promising for electrocatalytic applications [16]. Numerous SACs with these main-group metals anchored on graphene substrate have been successfully synthesized in experiments and applied in various catalytic reactions, for example, K [17], Mg [18], Ca [19], Al [20], Ga [21], In [22], Ge [23], Sn [24], Sb [25] and Bi [26]. It was also found that the coordination environment of the central metal atom has significant impact on the catalytic performance [27–29]. With a wide variety of central metals and doped heteroatoms, it makes experimental research labors and resources intensive to develop high-performance 2e⁻ ORR catalysts.

As we know, the density functional theory (DFT) method can provide robust theoretical guidance and computational data, and machine learning (ML) can efficiently learn and process data in large quantities [30–33]. Combining the advantages of both methods above, the research paradigm of integrating DFT and ML offers an efficient way for predicting potential catalysts. On one side, the theoretical prediction could provide crucial insights for experi-

* Corresponding authors.
E-mail addresses: yang.liu@hit.edu.cn (Y. Liu), hitliu@hit.edu.cn (G. Liu), yyuan@hit.edu.cn (Y. Yao).

https://doi.org/10.1016/j.cclet.2024.110711
1001-8417/© 2025 Published by Elsevier B.V. on behalf of Chinese Chemical Society and Institute of Materia Medica, Chinese Academy of Medical Sciences.

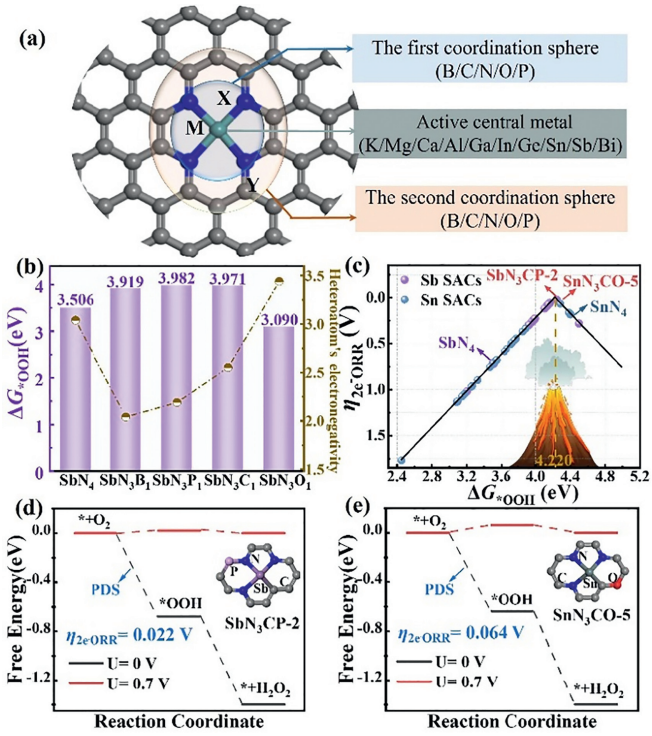


Fig. 1. DFT calculations results. (a) Structural diagram of SAC (denoted as $MN_aX_{4-a}Y$-b), with active central metal and the first/second coordination sphere layout, where M represents main-group metal of Group IA to VA; X, Y refer to the doped heteroatom in 1st sphere and 2nd sphere, respectively; a is the number of M-N ligand in 1st sphere and b is the site of doped atom in 2nd sphere. (b) The ΔG_{*OOH} of Sb SACs with different doped atoms in the first coordination sphere. (c) Volcano plot of Sb SACs and Sn SACs with the η_{2e^-ORR} plotted as a function of ΔG_{*OOH}. The free energy diagrams of 2e⁻ ORR pathway in (d) SbN_3CP-2 and (e) SnN_3CO-5.

ments endeavors and assist with the fast development of 2e⁻ ORR catalysts [34,35]. On the other side, the investigation of structure-activity relationship and descriptors will be informative for understanding catalytic mechanism further [36].

In light of the aforementioned above, we conducted the coordination engineering research for the main-group metal (from Group IA to VA) single-atom catalysts in this study. By doping with B/C/N/O/P atoms in the first and second coordination spheres, hundreds of single-atom catalysts with different characteristics were designed. Through the integration of DFT and ML, we utilized the strategy of electronegativity-oriented coordination regulation to identify the catalysts candidates with pretty good performance, and revealed intrinsic descriptors linking catalytic activity to electronic structure. This study provides valuable guidance for the designing and screening of promising hydrogen peroxide electrocatalysts.

The heteroatoms were introduced in the first/second coordination sphere positions of main-group metals (K, Mg, Ca, Al, Ga, In, Ge, Sn, Sb, Bi) with different ratios, resulting in a great deal of theoretical models (Fig. 1a and Fig. S1 in Supporting information). By choosing 89 representative models and employing the DFT method, we firstly calculated the binding energy (E_b) for evaluating the structural stability in thermodynamics. Guided by the well-known Sabatier principle, a promising electrocatalyst with a defined active center and geometric structure should bind adsorbed molecules with moderate strength. In the context of the 2e⁻ ORR, OOH is the key intermediate. To achieve high electrocatalysis performance, it is crucial to modulate the thermodynamic free energy of *OOH adsorption, aiming to reach the ideal value of 4.220 eV [37]. So the free energy of *OOH adsorption (ΔG_{*OOH}) is calculated for assessing the 2e⁻ ORR activity, and the produced data will be used for the following machine learning. The Sb and Sn SACs are illustrated here as representatives to illustrate two cases where introducing atoms with weak or strong electronegativity into coordination environment improves the catalytic performance of two-electron oxygen reduction reaction.

The Sb SAC with four N coordination atoms (denoted as SbN_4) was found in experiment to be a good catalyst of 4e⁻ ORR to produce water [25]. Our theoretical calculations indicate that its poor 2e⁻ ORR activity is due to the excessively strong adsorption for OOH intermediate and resulting very small ΔG_{*OOH} value of 3.506 eV, which is far from the ideal value of 4.220 eV. To improve its 2e⁻ ORR catalytic activity, we firstly introduce the heteroatom into the first coordination sphere of SbN_4 catalyst by substituting one N site with the B, C, O, or P atom. The E_b values are negative (lower than −2.40 eV), suggesting that the doping structures are thermodynamically stable. Fig. 1b shows the free energies of *OOH adsorption on these catalyst models. It can be observed that after doping B, C, P atoms with weaker electronegativity than N, the ΔG_{*OOH} increases and adsorption strength weakens. In comparison, after doping of O element with stronger electronegativity than N, the adsorption intensity of *OOH becomes stronger, which is unfavorable for the generation of hydrogen peroxide. Obviously, the electronegativity of introduced heteroatoms significantly impacts the strength of *OOH adsorption. Inspired by this, we continue to use B or P atom with weak electronegativity than carbon to change the second coordination sphere of SbN_3C_1, SbN_3P_1, and SbN_3B_1 catalysts. Depending on the distance between the active center and the surrounding sites, as described in the Supporting information, 12 catalysts were designed and found to show good thermodynamically stability. We analyzed the overpotential (η_{2e^-ORR}) and ΔG_{*OOH} of the above catalysts, and found that they showed perfect volcano type relationship in Fig. 1c. The catalyst SbN_3CP-2 with the C and P doped atom in the first and second coordination sphere, respectively, locates at the top of the volcano. The ΔG_{*OOH} on it reaches 4.242 eV and the overpotential is 0.022 V (Fig. 1d), suggesting extremely great activity for 2e⁻ ORR. In the case of Sb SACs, one can see that the doping of heteroatom with relatively weak electronegativity in the coordination environment could weaken the adsorption of OOH intermediate so as to improve the 2e⁻ ORR activity of the pristine SbN_4 which locates at the left slope of the volcano.

Different from the case of SbN_4 above, SnN_4 locates at the right side of the volcano with the relatively big ΔG_{*OOH} value of 4.401 eV, which also results in bad 2e⁻ ORR performance [24]. When introducing the heteroatoms, 27 Sn SACs models were considered and evaluated (Fig. S4 in Supporting information). From the volcano diagram in Fig. 1c, one can see that the SnN_3CO-5 shows the best 2e⁻ ORR activity with a very low overpotential of 0.064 V (Fig. 1e). Apparently, the doping of O atom with relatively strong electronegativity in the coordination environment plays an important role in tuning the activity of Sn SACs by enhancing the *OOH adsorption strength. As a short summary, through DFT calculations, we found a clue on the electronegativity magnitude of heteroatoms to modulate the coordination environment around different main-group metal center to obtain moderate adsorption ability for the OOH intermediate. As expected, it is confirmed to be an important thermodynamic activity descriptor by the following machine learning.

The distinguished tendency of *OOH adsorption intensity for Sb and Sn SACs by introducing different doped coordination atoms could be further explained by the crystal orbital Hamilton population (COHP) and projected density of states (PDOS) analysis. The ICOHP value was calculated by integrating the occupied energy of bonding or antibonding orbitals up to E_F. The greater ICOHP is, the weaker is the bonding interaction between active metal atom and

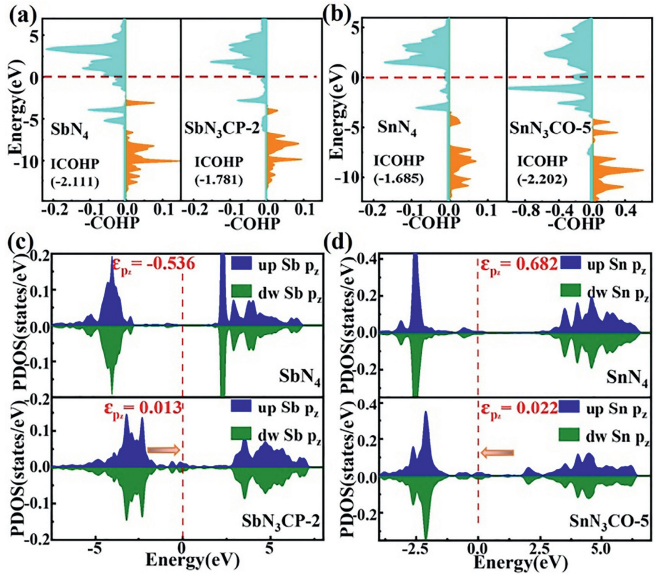


Fig. 2. Electronic structure analysis. COHP diagrams for *OOH adsorbed on (a) SbN_4 and SbN_3CP-2; (b) SnN_4 and SnN_3CO-5. PDOS diagrams of p_z orbital in (c) SbN_4 and SbN_3CP-2; (d) SnN_4 and SnN_3CO-5.

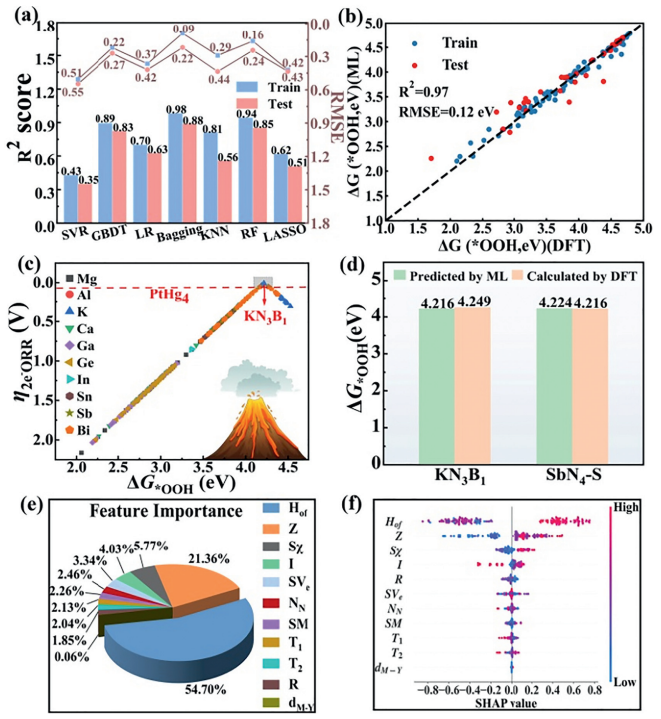


Fig. 3. Machine learning results. (a) The R^2 and RMSE values for the train set and test set by seven algorithms. (b) Gibbs free energy of *OOH adsorbed on SACs surface calculated by DFT and predicted by Bagging algorithm. (c) Volcanic relationship between ΔG_{*OOH} and η_{2e^-ORR} for 460 SACs plotted by the Bagging model prediction data. (d) Comparison of the ΔG_{*OOH} by DFT and ML for KN_3B_1 and SbN_4-S. (e) Percentage of feature importance. (f) Feature density scatter plot using SHAP method with the Bagging model.

O atom of OOH intermediate [38,39]. As shown in Figs. 2a and b, the variation of ICOHP values typically indicates a weakening of the Sb–O bond and a strengthening of the Sn–O bond, suggesting a tendency towards more moderate changes in adsorption strength. Fig. S5 (Supporting information) shows the DOS distribution of p orbital of Sb/Sn atom and the O atom of OOH. The orbital overlap mainly from the p_z orbital of main-group metal atom, which means that the p_z orbital is the main contributor to the *OOH adsorption intensity [40]. As illustrated in Figs. 2c and d, it can be seen that p_z-band center (ε_{pz}) of the catalysts with the incorporation of heteroatom is very close to the Fermi level, which is probably the reason for the moderate adsorption strength of *OOH. When C and P are introduced into coordination spheres, ε_{pz} shifts towards more positive energy relative to the Fermi level. This shift leads to weaker interaction between SbN_3CP-2 substrate and OOH intermediate. On the contrary, the incorporation of C and O in the coordination spheres results in a more negative shift of ε_{pz}, which indicates stronger interaction between SnN_3CO-5 substrate and OOH intermediate.

To expedite the development of main-group metal SACs for $2e^-$ ORR, a rapid prediction of ΔG_{*OOH} using atomic physicochemical parameters is essential. Using the calculated data mentioned above, along with additional data from the literature, we employed seven machine learning algorithms for training and optimized the model performance across various hyperparameters obtained by grid search and cross-validation. Some feature descriptors were initially proposed based on the chemical intuition, and then eleven characteristic quantities were ultimately determined through Pearson correlation analysis (Fig. S6 in Supporting information). Fig. 3a illustrates the R^2 and RMSE values for the train sets and test sets by the seven algorithms. Among them, the Bagging model shows the best predictive performance for the target values with $R^2 = 0.97$, RMSE = 0.12 eV (Fig. 3b). In Bagging model [41], by training multiple base learners on different data subsets and aggregating the results of these models, training variance is reduced successfully, thus enhancing model stability and improving generalization ability. Additionally, it could adapt to different data distributions to some extent through bootstrap sampling, allowing it to capture a wide range of data patterns. That could be the reason that Bagging algorithm shows impressive performance than others in present case.

Utilizing the well-trained Bagging model, the high-throughput screening is performed to predict promising catalysts. By inputting feature descriptors, the *OOH adsorption energies of the 460 single-atom catalysts of main-group metals can be obtained within seconds (Fig. 3c). Using $PtHg_4$ as a benchmark [9], sixteen catalysts demonstrate smaller overpotentials and excellent catalytic activity in Fig. S8 (Supporting information). They are all potential candidates for $2e^-$ ORR. The group of K SACs are very promising since many doped structures are near the top of the volcano. In particular, the KN_3B_1 has the best $2e^-$ ORR activity with overpotential of 0.029 V. It is expected that the present predictions will be informative for the experimental investigations in future. To validate the predictive accuracy of the training model, we conducted additional DFT calculations for the KN_3B_1 which was selected by ML. The calculated ΔG_{*OOH} of 4.249 eV by DFT is quite close to that of 4.216 eV from ML, as shown in Fig. 3d. In addition, taking use of the Bagging model, we predict the experimentally feasible porphyrin-based Sb SAC with doped S atom (denoted as SbN_4-S) to be a good $2e^-$ ORR catalyst due to the appropriate ΔG_{*OOH} of 4.224 eV, which also matches well with the DFT result in literature [42]. Both of the examples above strongly convinced the reliability of the machine learning model trained in this study.

Additionally, feature importance is extracted from the trained Bagging model using the SHapley Additive exPlanations (SHAP) method. As shown in Fig. 3e, the top three most important descriptors are enthalpy of oxide generation of metal (H_{of}, 54.70 %), atomic number of metal (Z, 21.36 %), and the sum of electronegativity of all coordination atoms in the 1st and 2nd sphere ($S\chi$, 5.77 %). Fig. 3f displays the impact of each input feature on the model output for the whole 1914 data points in the order of feature importance, col-

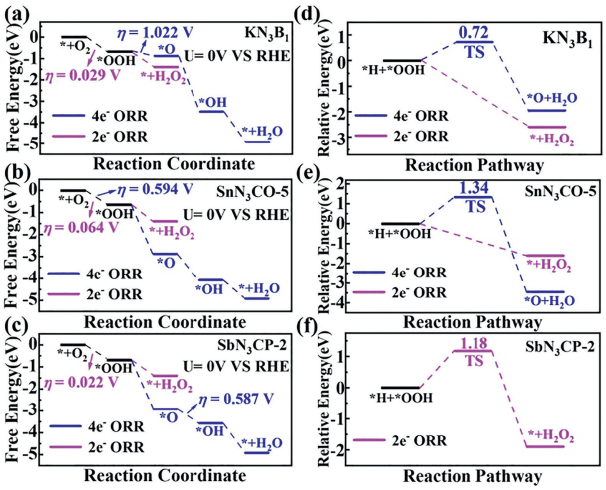


Fig. 4. Reaction selectivity and dynamic behavior. Gibbs free energy diagrams of oxygen reduction reactions for (a) KN_3B_1, (b) SnN_3CO-5, (c) SbN_3CP-2, and corresponding dynamic barriers of key steps for (d) KN_3B_1, (e) SnN_3CO-5, (f) SbN_3CP-2.

ored based on the feature values. This indicates that the higher values of H_{of}, Z and Sχ possess higher SHAP values with a higher positive impact on the model output, while the distributions for the remaining features are mostly centered on a SHAP value of zero, indicating low importance and minimal impact on most results. The first two descriptors are closely related to the central metal element, so they contribute the most to the catalytic activity. Once the central metal atom is fixed, the *OOH adsorption energy is primarily determined by the electronegativity of the coordinating atoms in the 1st and 2nd sphere, successfully confirming the DFT calculation results and aligning with the electronegativity regulation strategy above. Therefore, the combined DFT and ML research paradigm propose the importance of regulation strategy of electronegativity-based coordination environment for single atom electrocatalysts in 2e- ORR.

Based on the predictions above, we can efficiently screen out the highly active hydrogen peroxide catalysts from the viewpoint of thermodynamics. However, the selectivity of the catalysts, *i.e.*, the influence from the competing reaction of four-electron oxygen reduction reaction (4e- ORR) to produce water, should be fully considered. But the lack of sufficient dynamic data makes the ML temporarily powerless. Therefore, the further study on catalytic selectivity is conducted by DFT.

We choose three catalysts with the best thermodynamic activity for K, Sn and Sb SACs. The complete Gibbs free energy diagram for 2e- and 4e- ORR pathways are shown in Figs. 4a-c. As we can see, the potential-determining step in the four electron pathway of KN_3B_1 is the process of *OOH to *O with overpotential of 1.022 V and that of SnN_3CO-5 is the first step of activating oxygen to produce the intermediate *OOH with overpotential of 0.594 V, respectively. On SbN_3CP-2, the potential-determining step is the hydrogenation process of *O to *OH with overpotential of 0.587 V. Therefore, the three catalysts show bad 4e- ORR thermodynamic activity with high overpotential. In order to further explore the selectivity of catalysts, the transition state (TS) is searched for the key hydrogenation step of *OOH to H_2O_2 (2e- ORR) or *O + H_2O (4e- ORR), and the activation barriers are obtained. From Figs. 4d-f, we can see that the 2e- ORR processes on catalysts KN_3B_1 and SnN_3CO-5 are barrier-free while the barrier of 4e- ORR is 0.72 and 1.34 eV, respectively, indicating the outstanding dynamic advantages of 2e- ORR. In contrast, on SbN_3CP-2, the 2e- ORR dynamic barrier is as high as 1.18 eV, suggesting the extreme difficulty to generate hydrogen peroxide. Overall, it is determined that the KN_3B_1 and SnN_3CO-5 catalysts have impressive activity and selectivity for 2e- ORR, presenting a promising option for future electrocatalytic hydrogen peroxide synthesis. Additionally, we evaluated the thermal and structural stability of these two catalysts through ab initio molecular dynamics (AIMD) simulations for 20,000 fs at 1000 K (Fig. S10 in Supporting information). The temperature, energy and bond length fluctuates in a very narrow range, indicating the high thermodynamic stability of KN_3B_1 and SnN_3CO-5 catalysts. Note that in a practical electrochemical environment, the performance of catalysts could be influenced by many factors, such as the solvation effect and electrostatic potential. Therefore, we employed implicit solvation model [43] and the constant potential charge extrapolation method [44,45] to evaluate the impact of solvation effect and electrode potential on the reaction energies on KN_3B_1 and SnN_3CO-5 catalysts, respectively. As shown in Fig. S11, Tables S3 and S4 (Supporting information), they are within an acceptable margin of error, indicating that these two factors have minimal impact on the theoretical prediction and identification of promising electrocatalyst candidates. Furthermore, previous experimental studies have shown that KN_4 and SnN_4 can be successfully synthesized [17,24], and the methods for incorporating B or O atom into the coordination environment of SACs were well-established [46,47], which greatly boost the feasibility of synthesizing KN_3B_1 and SnN_3CO-5 in experiment.

In summary, by combining DFT and ML methods, we studied a series of main-group metal single-atom catalysts with adjustable coordination environment for two-electron oxygen reduction reaction to generate H_2O_2. The KN_3B_1 and SnN_3CO-5 were screened out to display promising activity and selectivity for 2e- ORR among 566 candidates. The Bagging algorithm demonstrated significant advantages in this system due to its effective ensemble strategy. Based on the feature importance analysis of this model, we elucidated the importance of the electronegativity of the coordination atoms in describing the catalytic performance of SACs. This research paradigm of integrating DFT and ML maximizes the strengths of both approaches, promotes the efficiency of catalyst development, and demonstrates significant potential in the fields of materials science and catalysis.

Declaration of competing interest

The authors declare that they have no known competing financial interests or personal relationships that could have appeared to influence the work reported in this paper.

CRediT authorship contribution statement

Hao Chen: Writing – review & editing, Writing – original draft, Investigation, Formal analysis, Data curation, Conceptualization. **Haiyuan Liao:** Investigation, Formal analysis. **Qi Zhou:** Writing – review & editing, Investigation. **Yang Liu:** Writing – review & editing, Writing – original draft, Supervision, Software, Project administration, Investigation, Formal analysis, Data curation, Conceptualization. **Guojun Liu:** Writing – review & editing, Supervision, Investigation, Data curation. **Yuan Yao:** Writing – review & editing, Supervision, Investigation, Funding acquisition, Data curation.

Acknowledgment

This work was supported by the National Natural Science Foundation of China (Nos. U2067216, 61976071).

Supplementary materials

Supplementary material associated with this article can be found, in the online version, at doi:10.1016/j.cclet.2024.110711.

References

[1] H.W. Kim, M.B. Ross, N. Kornienko, et al., Nat. Catal. 1 (2018) 282–290.
[2] J.M. Campos-Martin, G. Blanco-Brieva, J.L.G. Fierro, Angew. Chem. Int. Ed. 45 (2006) 6962–6984.
[3] Z.W. Seh, J. Kibsgaard, C.F. Dickens, et al., Science 355 (2017) 1.
[4] P. Lang, N.N. Yuan, Q.Q. Jiang, et al., Energy Technol. 8 (2020) 18.
[5] K.Y. Chen, Y.X. Huang, R.C. Jin, B.C. Huang, Appl. Catal. B: Environ. Energy 337 (2023) 19.
[6] J. Xie, L. Zhong, X. Yang, et al., Chin. Chem. Lett. 35 (2024) 108472.
[7] M. Liu, X. Xiao, Q. Li, et al., J. Colloid. Interf. Sci. 607 (2022) 791–815.
[8] Z.Q. Deng, L. Li, Y.C. Ren, et al., Nano Res. 15 (2022) 3880–3885.
[9] S. Siahrostami, A. Verdaguer-Casadevall, M. Karamad, et al., Nat. Mater. 12 (2013) 1137–1143.
[10] A. Verdaguer-Casadevall, D. Deiana, M. Karamad, et al., Nano Lett. 14 (2014) 1603–1608.
[11] J.K. Edwards, G.J. Hutchings, Angew. Chem. Int. Ed. 47 (2008) 9192–9198.
[12] R. Chattot, O.Le Bacq, V. Beermann, et al., Nat. Mater. 17 (2018) 827.
[13] Y.Q. Wang, J.Y. Hao, Y. Liu, et al., J. Energy Chem. 76 (2023) 601–616.
[14] J. Li, S.G. Chen, N. Yang, et al., Angew. Chem. Int. Ed. 58 (2019) 7035–7039.
[15] H.Y. Sheng, R.D. Ross, J.R. Schmidt, S. Jin, ACS Energy Lett. 8 (2022) 196–212.
[16] H. Wang, Y.J. Zhao, J. Li, et al., Small Struct. 4 (2023) 11.
[17] N.K. Guo, H. Xue, R. Ren, et al., Angew. Chem. Int. Ed. 62 (2023) e202385061.
[18] S. Liu, Z. Li, C. Wang, et al., Nat. Commun. 11 (2020) 938.
[19] Z.Y. Lin, H. Huang, L. Cheng, et al., Adv. Mater. 33 (2021) 10.
[20] C.Q. Zhuang, W.M. Li, T.Y. Zhang, et al., Nano Energy 108 (2023) 12.
[21] Z.D. Zhang, J.X. Zhu, S.H. Chen, et al., Angew. Chem. Int. Ed. 62 (2023) e202303117.
[22] J.W. Zhang, G.M. Zeng, L.L. Chen, et al., Nano Res. 15 (2022) 4014–4022.
[23] M. Tripathi, A. Markevich, R. Böttger, et al., ACS Nano 12 (2018) 4641–4647.
[24] F. Luo, A. Roy, L. Silvioli, et al., Nat. Mater. 19 (2020) 1215–1223.
[25] T. Wang, X. Cao, H. Qin, et al., Angew. Chem. Int. Ed. 60 (2021) 21237–21241.
[26] X.P. Yang, Y.L. Chen, L. Qin, et al., ChemSusChem 13 (2020) 6307–6311.
[27] Y. Yan, H. Qu, X. Zheng, et al., Chin. Chem. Lett. 33 (2022) 4655–4658.
[28] Y.Z. Zhu, J. Sokolowski, X.C. Song, et al., Adv. Energy Mater. 10 (2020) 29.
[29] X. Lu, Y. Chang, S. Wang, et al., Chin. Chem. Lett.36 (2025) 110277.
[30] H. Sun, Y.Z. Li, L.Y. Gao, et al., J. Energy Chem. 81 (2023) 349–357.
[31] C.Z. Pan, M. Mahmoudabadbozchelou, X.L. Duan, et al., J. Colloid. Interf. Sci. 611 (2022) 29–38.
[32] Z.Z. Liang, H.B. Guo, H.T. Lei, R. Cao, Chin. Chem. Lett. 33 (2022) 3999–4002.
[33] H. Li, S.P. Xu, M. Wang, et al., J. Mater. Chem. A 8 (2020) 17987–17997.
[34] X. Zhang, K. Li, B. Wen, et al., Chin. Chem. Lett. 34 (2023) 107833.
[35] L.P. Wu, T. Guo, T. Li, Adv. Funct. Mater. 32 (2022) 10.
[36] Y.R. Jiao, H.B. Li, Y. Jiao, S.Z. Qiao, J. Am. Chem. Soc 145 (2023) 15572–15580.
[37] X.Y. Guo, S.R. Lin, J.X. Gu, et al., ACS Catal. 9 (2019) 11042–11054.
[38] R. Nelson, C. Ertural, J. George, et al., J. Comput. Chem. 41 (2020) 1931–1940.
[39] S. Steinberg, R. Dronskowski, Crystals 8 (2018) 26.
[40] W. Pei, S. Zhou, Y.Z. Bai, J.J. Zhao, Carbon 133 (2018) 260–266.
[41] L. Breiman, Mach. Learn. 24 (1996) 123–140.
[42] M. Yan, Z. Wei, Z. Gong, et al., Nat. Commun. 14 (2023) 368.
[43] K. Mathew, R. Sundararaman, K. Letchworth-Weaver, et al., J. Chem. Phys. 140 (2014) 8.
[44] K. Chan, J.K. Norskov, J. Phys. Chem. Lett. 6 (2015) 2663–2668.
[45] K. Chan, J.K. Norskov, J. Phys. Chem. Lett. 7 (2016) 1686–1690.
[46] E.H. Zhang, L. Tao, J.K. An, et al., Angew. Chem. Int. Ed. 61 (2022) e 2 0 2 2 01 4 9 4.
[47] B.R. Wulan, X.Y. Cao, D.X. Tan, et al., CCS Chem. 5 (2023) 2415–2425.